CrystEngComm

View Online
Dynamic Article Links

Cite this: *CrystEngComm*, 2011, **13**, 1111

www.rsc.org/crystengcomm

PAPER

Monosodium urate monohydrate crystallization

Clare M. Perrin,[a] Mark A. Dobish,[b] Edward Van Keuren[b] and Jennifer A. Swift*[a]

Received 19th October 2010, Accepted 8th December 2010
DOI: 10.1039/c0ce00737d

The crystallization of monosodium urate monohydrate (MSU) in the synovial fluid has long been associated with the joint disease gout, which is characterized by recurring attacks of pain and inflammation within the joints. In this work, *in situ* atomic force microscopy (AFM) on single crystal (010) MSU surfaces and dynamic light scattering were used complementarily to investigate the growth of MSU in 2–10 mM urate solutions under model physiological conditions (37 °C, pH = 7.4, 150 mM NaCl). In this solution regime, crystal growth rates normal to the (010) surface followed the square of supersaturation, which is consistent with a two-dimensional island nucleation and spread mechanism. Islands observed under *in situ* AFM imaging conditions had sizes consistent with dynamic light scattering measurements but exhibited unique faceting not typically observed in fully developed crystals or predicted by previous theoretical work. Preferred alignment of the islands' long axis and the underlying $\pm c$ axis of the MSU (010) was observed, as was island overgrowth over time.

Introduction

The crystal deposition disease gout is characterized by recurring attacks of severe joint pain and inflammation, most commonly in the big toe, instep, ankles, heels, knees, wrists, fingers, and elbows,[1] triggered by the presence of monosodium urate monohydrate (MSU) crystals in the synovial fluid. Historically, gouty arthritis has been associated with males and overindulgent lifestyles; however, the modern day occurrence of gout affects a wider demographic, including females and a range of socioeconomic groups.[2] Gout is often encountered in conjunction with other conditions such as metabolic syndrome, obesity, diabetes mellitus, hypertension, and coronary heart disease.[3–5] Isolated gout attacks may also be triggered by specific events such as trauma, surgery, excessive alcohol intake, or drugs that affect serum urate levels.[6]

Urate, the ionized form of uric acid ($pK_{a1} = 5.5$)[7] formed by deprotonation at N3, is a normal metabolic byproduct of purine metabolism. Physiologic serum is tightly regulated at pH = 7.4 at 37 °C. Under these conditions, urate is the predominant form of uric acid in solution and sodium is the most abundant counterion (150 mM). Changes to these optimized conditions can affect the relative solubility of urate. Hyperuricemia, defined as a blood serum urate level at or above 7.0 mg per 100 mL or 0.42 mM,[1,5] is a necessary but non-exclusive precondition for the crystallization of MSU *in vivo*. Most cases of hyperuricemia result from either the overproduction or underexcretion of uric acid, the latter being more prevalent.[2,8] The presence of other MSU crystal growth promoters or the lack of growth inhibitors may also play a physiological role since not all hyperuricemic patients develop gout.

Bulk growth rates have been previously measured for MSU.[9–17] Different growth mechanisms were proposed based on studies conducted under similar conditions. For example, Lam Erwin and Nancollas[11] advocated a spiral growth mechanism, while Calvert *et al.*[9] reported a two-dimensional island nucleation mechanism. One potential complicating factor in these studies was the high urate supersaturation level used ([urate] = 15.4 mM). These conditions were necessary to obtain measurable growth rates using potentiometric[11] and light microscopy methods,[9] but are well above the typical urate concentration ranges found in physiologic environments.

In situ atomic force microscopy (AFM) is a sensitive technique for investigating the molecular-level surface growth and dissolution processes on single crystal surfaces. The growth of molecular crystals implicated in other crystal deposition diseases has been investigated using such methods, including studies on cholesterol,[18] anhydrous uric acid,[19] calcium oxalate[20–22] and cysteine.[23] In the present work, the molecular-level growth of MSU single crystals is investigated as a function of supersaturation at pH = 7.4 and 37 °C, using *in situ* AFM on (010) single crystal surfaces and dynamic light scattering (DLS). These complementary methods provide an unprecedented molecular level insight into the mechanistic aspects of MSU growth under model conditions.

[a]*Department of Chemistry, Georgetown University, 37th and "O" Streets, NW Washington, DC, 20057-1227, USA. E-mail: jas2@georgetown.edu; Fax: +1 (202) 687-6209; Tel: +1 (202) 687-5567*
[b]*Department of Physics, Georgetown University, 37th and "O" Streets, NW Washington, DC, 20057, USA; Fax: +1 (202) 687-2087; Tel: +1 (202) 687-5982*

Experimental

MSU sample preparation

MSU crystals were obtained by adding 1.250 mL 1 M NaOH, 168.1 mg of uric acid (Sigma, 99%, used without further purification) and 818.6 mg NaCl to gently heated and stirred 100 mL solutions of distilled H_2O. The mixture was gravity filtered using Whatman #1 paper, distributed among four vials and placed in a 37 °C water bath. The uric acid and base concentrations used (10 mM and 12.5 mM, respectively) were empirically optimized to provide the thickest needles possible for AFM analysis. The MSU crystals obtained typically grew in 2–3 days and were ~100 to 200 μm in length and 10 to 20 μm in width across the largest side face.

To prepare MSU crystals for AFM imaging, a glass coverslip was washed in acetone, dried in a 100 °C oven for 5 minutes, and coated with a thin layer of UV-curable glue (Type SK-9, EMS Acquisition Corp.) spread with a razor edge. The coverslip was partially cured for 10 minutes under a UV lamp (Model UVL-56, EMS Acquisition Corp.) before a drop of the crystal solution was placed on top. After 1–2 minutes, the excess solution was wicked off leaving MSU crystals in multiple orientations adhered to the coverslip. Coverslips were cured for an additional 20 minutes and then inspected by optical microscopy. All crystals selected for AFM analysis appeared free of debris and visible defects and were at least 10 μm wide.

In situ Atomic Force Microscopy (AFM)

All AFM experiments were performed on a Nanoscope IIIa Multimode instrument (Digital Instruments) equipped with a temperature controlled fluid cell and a custom built temperature controlled fluid reservoir operated in contact mode. A J scanner (max scanning area = 30 μm^2) and Si_3N_4 cantilevers (spring constant = ~0.3 N m^{-1} and length = 100 μm) were used. A glass coverslip with mounted MSU crystals was adhered to a stainless steel puck with epoxy and oriented in the AFM fluid cell so that the long needle axis of MSU was aligned parallel to the fast scan x-direction.

The AFM growth solutions were prepared by heating 100 mL of distilled water with 818.6 mg NaCl and adding varying equimolar amounts of 1 M NaOH and uric acid to achieve the desired concentration range (up to 10 mM). The solution was buffered to pH = 7.4 using sodium dihydrogen phosphate monobasic and sodium hydrogen phosphate dibasic. The solution was gravity filtered using Whatman #1 paper and maintained in a 50 °C water bath. All solutions were used within two hours of preparation.

Supersaturated urate solution from a heated fluid reservoir held at 40.0 (±0.1) °C was drawn through short silicon tubing into the fluid cell at a constant flow rate of 5 mL h^{-1} using a syringe pump (KD Scientific model KDS210). At this flow rate, the solution inside the cell was completely exchanged every 36 min, thereby ensuring diffusion controlled growth. The fluid cell temperature was maintained at 37 °C and monitored using an Omega thermocouple directly inserted into the fluid cell. Supersaturation inside the cell was controlled by varying the concentration of the growth solution. The equilibrium equation is represented below:

$$NaU \cdot H_2O_{(s)} \leftrightarrow Na^+_{(aq)} + U^-_{(aq)} + H_2O_{(l)}$$

where NaU corresponds to sodium urate and U^- is the dissociated urate anion.

Growth was examined in 2–10 mM urate/150 mM NaCl solutions. AFM images obtained in 4 mM urate/150 mM NaCl showed neither growth nor dissolution. Solutions of <4 mM urate consistently showed dissolution. Solutions of >4 mM urate showed consistent growth, though imaging solutions of >8 mM urate was complicated by high levels of spontaneous nucleation which were difficult to control reliably. The ionic strength of the solution, $I = 0.15$, was essentially constant over the entire range.

Scanning Electron Microscopy (SEM)

All SEM experiments were performed on a Zeiss SUPRA 55-VP scanning electron microscope (Zeiss, Germany) operated in vacuum. Scanning electron micrographs were collected using an accelerating voltage of 0.50 kV. All samples were mounted on 12 mm double stick carbon circles (M. E. Taylor Engineering, Inc.), which were affixed on 1/8 inch SEM mount pins (M. E. Taylor Engineering, Inc.).

Dynamic Light Scattering (DLS)

All DLS experiments were conducted at 37 °C. The temperature was controlled by a Grant LTD-6 water bath system set to 42 °C, which was connected to a water-jacketed cuvette (Hellma type 161). A flow control valve built into the water circulation system efficiently controlled the water flow rate (~1 to 2 mL s^{-1}), protected the cuvette from additional water pressure, and resulted in a temperature of 37 °C inside the sample chamber. All measurements were taken on samples prepared in triplicate.

Data were obtained using either a helium–neon (HeNe) laser or a laser diode (Hitachi HL6548FG) controlled by a ThorLabs LDC2000 laser diode power supply. The HeNe laser (10 mW power, $\lambda = 632.8$ nm) was used primarily for higher concentration solutions (>5 mM urate), while the diode laser (90 mW power, $\lambda =$ 661 nm) was used for the lower concentration solutions (1–4 mM urate). The laser diode was mounted on a thermoelectrically cooled mount and maintained at a constant temperature. Scattered light measured at a 90° relative to the incident beam was filtered with a narrow bandpass optical filter and collected by a single mode optical fiber. Single mode waveguiding ensures that the measured signal is spatially coherent, which optimizes the signal to noise ratio of the autocorrelation function.

The other end of the single mode fiber was coupled to a photon counting avalanche photodiode (EG&G). The photon count rates were processed by an ALV5000 (ALV GmbH, Germany) hardware autocorrelator board. The photon count autocorrelation function was directly analyzed from the data using the method described by Frisken and Patty.[24,25] A nonlinear fitting routine was used to fit the function in eqn (1)

$$g^{(2)}(\tau) = B + \beta \cdot e^{-2\Gamma\tau} \cdot \left(1 + \frac{\mu_2}{2!}\tau^2 - \frac{\mu_3}{3!}\tau^3 \ldots\right)^2 \quad (1)$$

to the measured data where β is a factor that depends on the experimental geometry (coherence area of the detector), Γ, μ_2

and μ_3 are the first, second and third moment of the distribution of decay times, and B is a background term. Since most of the data were close to single exponential functions, only the first and second moments were used in the data analysis. The radius was determined from the fitted value for Γ. The diffusion coefficient, D, was found from the relation

$$\Gamma = Dq^2 \quad (2)$$

where q is the magnitude of the scattering vector, and is equal to eqn (3).

$$q = (4\pi n/\lambda_0)\sin(\theta/2) \quad (3)$$

The hydrodynamic radius was calculated from the Einstein–Stokes equation (eqn (4)) where k is the Boltzmann's constant ($=1.38 \times 10^{-23}$ J K^{-1}), T is the temperature (K), η is the dynamic viscosity (corrected for temperature), and R_h is the hydrodynamic radius of the particle.

$$D = kT/6\pi\eta R_h \quad (4)$$

The values of Γ and μ_2 were used to find the polydispersity index (PDI) (eqn (5)), a normalized measure of the width of the particle size distribution.

$$\mathrm{PDI} = \mu_2/\Gamma^2 \quad (5)$$

A PDI of zero implies a monoexponential decay to the autocorrelation function, which signifies a single diffusion coefficient.

Results and discussion

The structure of MSU (ref. code: NAURAT) was established in 1976 by Mandel and Mandel.[26] MSU crystallizes in the triclinic space group $P\bar{1}$, with unit cell dimensions a = 10.888 Å, b = 9.534 Å, c = 3.567 Å, $\alpha = 95.06°$, $\beta = 99.47°$ and $\gamma = 97.17°$.[26] The 3-dimensional structure consists of one-dimensional stacks of closely spaced (3.28 Å) purine rings oriented parallel to the c-axis (Fig. 1). Each urate also coordinates to a sodium ion *via* short Na···O electrostatic interactions and to water molecules through O–H···O and N···H–O hydrogen bonds. The coordination is responsible for the 7.7° twist of the urate ions out of the $(1\bar{1}0)$ plane.

A number of growth protocols for MSU have been reported,[9,11,13,15,26,27] all of which result in macroscopic crystals with needle-like morphologies elongated along the c-axis. MSU crystals suitable for AFM experiments were grown by heating aqueous solutions of 1 M NaOH, uric acid and NaCl until fully dissolved, then maintaining the temperature at 37 °C for 2–3 days. MSU crystals obtained from these conditions were typically 100–200 μm in length and 10–20 μm in width across the largest side face. A representative lab-grown crystal is shown in Fig. 2. The broad, flat side face of the needle was assigned by optical goniometry as (010), which is consistent with earlier reports.[26] The other side faces correspond to (100) and $(1\bar{1}0)$, and the fastest growing (001) face caps off the needle.

Light scattering of urate solutions

Dynamic light scattering (DLS) experiments were performed at 37 °C on 0–10 mM urate/150 mM NaCl solutions buffered to pH = 7.4. These are the same solution compositions used in *in situ* AFM growth experiments. After an equilibration time of 2–3 min, DLS measurements were acquired every 15 seconds for a total of ~50 minutes for each solution. In general, the number and average size of particles increased with urate concentration up to ~8 mM, at which point particle settling led to a decrease in the average size. DLS average particle sizes obtained under each

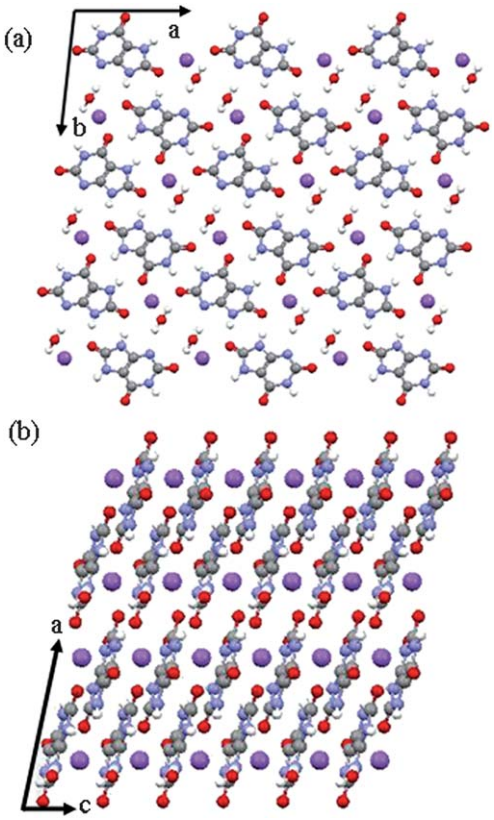

Fig. 1 (a) Schematic of needle-like MSU crystal showing end and side faces. (b) Packing diagram of MSU viewed along the c axis. (c) Packing diagram of MSU viewed along the b axis. Crystallographic axes are indicated. Packing diagrams created with Mercury with coordinates obtained from Mandel and Mandel.[26]

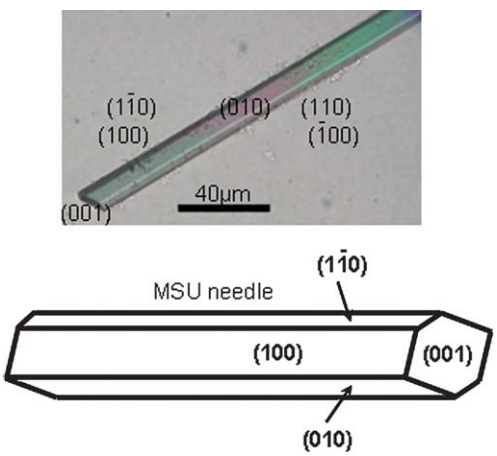

Fig. 2 Micrograph of a typical MSU crystal grown from basic aqueous conditions.

set of solution conditions were 0.56 μm (2 mM urate), 0.75 μm (3 mM), 0.93 μm (5 mM), 2.01 μm (7 mM), 2.65 μm (8 mM), 0.70 μm (9 mM), and 0.43 μm (10 mM). These values are in good agreement with the island sizes observed in AFM images. Representative particle size plots in 2, 5, 8 and 10 mM urate solutions are shown in Fig. 3.

In 2 mM urate solutions, all scattering is at the baseline (Fig. 3a). A handful of spikes are observed in the 2000–3000 nm range. Similar features have been interpreted by others[28–33] as the formation of dense liquid droplets of aggregated particles, which can dissolve easily back into the under-saturated solution. Increasing the $[urate]_{sol'n}$ to 5 mM resulted in a significant increase in the number of particles detected as compared to the 2 mM solution (Fig. 3b). In 8 mM urate solutions, the number of particles is significantly higher, suggesting that the particle lifetime is also increased. The average particle size also reaches a maximum at this concentration, with some exceeding 5000 nm.

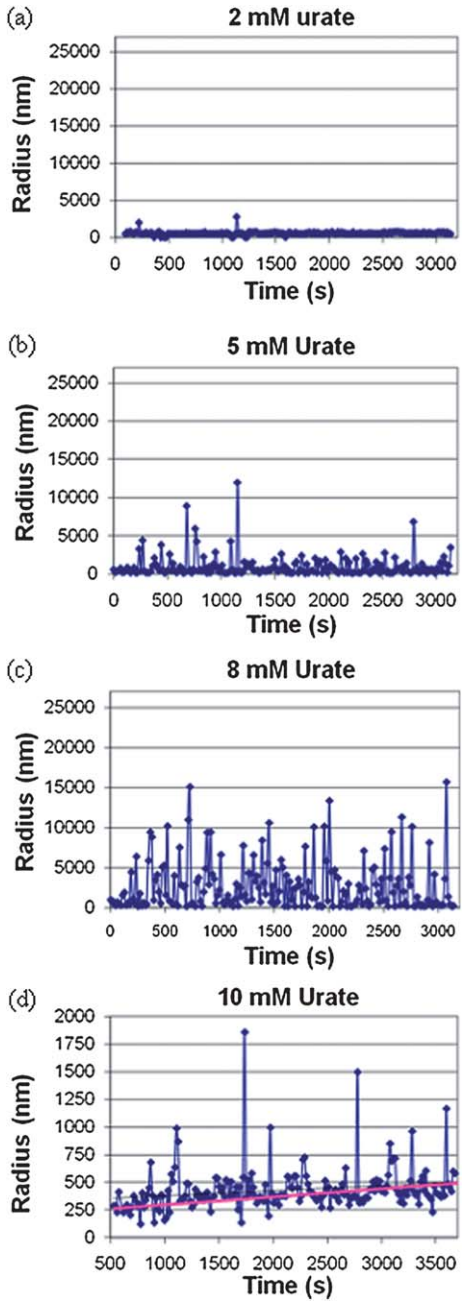

Fig. 3 DLS experiments of urate growth solutions at different saturation levels. [urate] = (a) 2 mM, (b) 5 mM, (c) 8 mM and (d) 10 mM. As [urate] increases, the number and size of particles in solution also increase in (a–c). In 10 mM urate solutions, the baseline has an upward slope, indicating the presence of stable growing particles in solution (d).

In the most concentrated urate solution examined, 10 mM (Fig. 3d), the average particle size appears reduced, though this is more likely due to the settling of larger, more stable particles on the bottom of the sample vial (noticeable after data collection) which do not pass through the instrument beamline. Notable is the fact that the baseline in the 10 mM urate data shows an increasing slope (indicated by the pink trendline). Literature precedent[29–31] has interpreted this slope to be indicative of a regime where stable crystal nuclei grow in solution.

In situ AFM growth on (010)

MSU (010) single crystal surfaces were initially imaged in aqueous solution under *in situ* AFM conditions to determine their topographical profiles. AFM imaging of MSU (010) was typically performed with the fast scan direction aligned parallel to the long axis of the needle (*c*-axis), though data collected on some sample crystals rotated by 90° were also performed to ensure that the tip scanning direction did not affect the growth. The smallest measured step heights were ~9.5 Å, which is in good agreement with the calculated inter-planar spacing between (0*k*0) planes, 9.40 Å. This value corresponds to one unit cell or two layers of urate molecules, and provides additional confirmation that the imaged face is in fact (010). (Minimum step heights on the other (100) and (1$\bar{1}$0) side faces have heights of 10.6 Å and 13.2 Å, respectively, based on the calculated inter-planar spacings.)

Sequential AFM images were collected on MSU (010) surfaces exposed to flowing urate solutions in an effort to monitor growth at the molecular-level. In all experiments performed with [urate] > 4 mM, growth was readily and consistently observed. AFM image series obtained in solutions with [urate] = 4 mM typically showed neither growth nor dissolution, and those with [urate] < 4 mM showed consistent dissolution. That said, even in solutions with ≤4 mM urate, the sudden appearance of islands was seen in some image sequences. This is consistent with DLS data which showed a detectable scattering at these same concentrations. When observed, all islands expressed an elongated prismatic or needle-like morphology ranging from 0.1–2.5 μm in the largest dimension. The long axis of the island and the *c*-axis of the underlying MSU substrate were also usually in parallel or near-parallel alignment.

Analysis of topographical changes across several growth experiments enabled some general mechanistic descriptions and kinetic parameters to be deduced. Fig. 4 illustrates the typical evolution of a (010) MSU surface over time in a flowing 7 mM urate/150 mM NaCl solution. Initially, the surface was fairly smooth, with an RMS roughness of 1.0 nm and surface steps ranging 1–5 nm in height. Within 8 minutes a macroscopic island, initially ~2 μm in length and 175 nm in height, appeared on the MSU surface. The major face of the island exposed could be assigned as (010), based on the direct measurement of mono- and multilayer steps on the island surface.

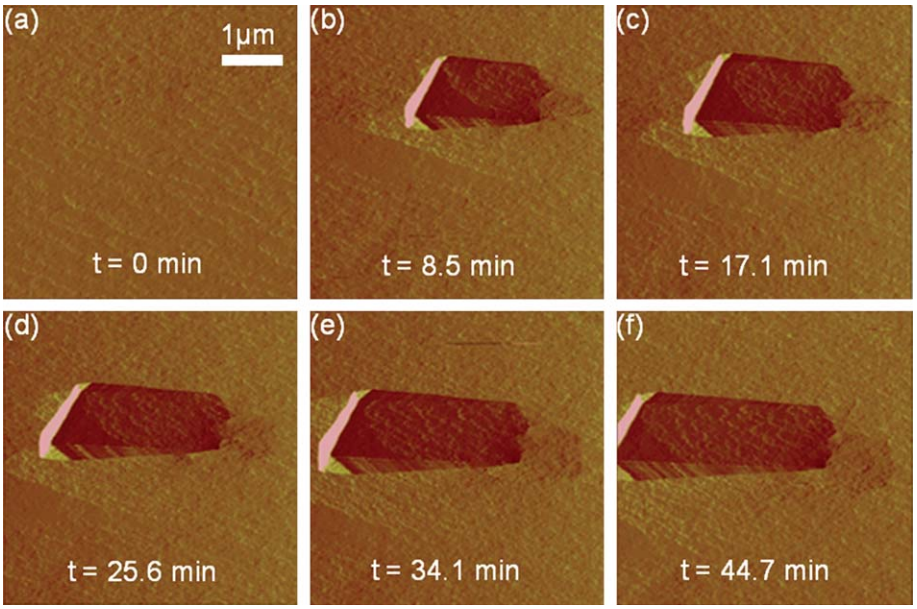

Fig. 4 Typical time-resolved *in situ* topographical image sequence of a MSU (010) surface growing in 7 mM urate/150 mM NaCl at 37 °C. A large island adsorbs from solution onto the MSU surface within the first 8 minutes (b) and then grows anisotropically over time (c–f).

Images (Fig. 4c–f) reveal the highly anisotropic growth of this island over time. After ~45 minutes, the island approximately doubled in length to ~4 μm, with all of the growth occurring from the left side. The growth anisotropy observed along $\pm c$ is not due to any intrinsic kinetic differences along this axis, but rather can be attributed to the fact that the island and substrate are slightly misaligned along Z. (MSU is centrosymmetric and in other image series, island growth along $\pm c$ directions occurs at similar rates.) From the time the island first appears, its right side seems to be partially embedded in the substrate, which presumably hinders its growth from that side. Over the ~36 min elapse between Fig. 4b and f, both the underlying substrate and the island grew in the Z-direction, albeit at different rates. This is reflected in a decrease in the island height relative to the substrate from 175 nm to 50 nm (left side measurement) over this time period.

With additional time, the island in Fig. 4 was overgrown by the substrate (not shown). This behavior is typical for new islands, which eventually become incorporated into the growing crystal surface under these solution conditions. The disappearance of islands, either through desorption or dissolution, was seen infrequently and typically only for the smallest islands. The loss of weakly attached islands may in some cases be related to the raster scanning of the tip.

The "island incorporation time" varied depending on both the size of the island and the solution supersaturation. In general, larger islands required more time to incorporate, and islands of a similar size were overgrown more quickly in higher supersaturation solutions. The calculated surface roughness values measured before island appearance and after island incorporation were essentially identical, ranging from about 1.0–1.4 nm. Images collected after island overgrowth rarely showed any indication of their unusual growth history.

There are at least two possible explanations for the sudden appearance of islands. They could be formed in solution and adsorbed onto the surface, or they might result from unusually fast growth of a slightly misaligned growth unit emerging from the underlying crystal surface. These two options are difficult to distinguish experimentally. That islands do occasionally appear in [urate] < 4 mM solutions when usually only surface dissolution is observed supports a solution-adsorption model, however, the fact that an island's long axis aligns with the c-axis of the underlying MSU substrate suggests the substrate plays a role as well.

Fig. 5 is a growth series obtained under flowing 6 mM urate/150 mM NaCl solution. The substrate is rotated 90° relative to that in Fig. 4 (*i.e.* the c-axis in Fig. 5 is vertical). When an island first spontaneously appeared on the surface (Fig. 5a), however, it initially was not perfectly aligned with the substrate. As a growth hillock from the left approaches and the two features come into contact, the hillock seemed to reorient the island moving the long axis into alignment with the underlying substrate in the subsequent image. The island is overgrown in the following ~45 minutes by multilayers from the left and below and a large macrostep approaching from the right. No obvious signs of island overgrowth were apparent on the surface in images obtained several minutes later (not shown).

Growth rates normal to the MSU (010) surface were extracted from sequential AFM images collected on larger areas by measuring the absolute height of the macroscopic crystal relative to the glass substrate upon which it was mounted. Plots of Δheight *vs.* time displayed a second order polynomial dependence (Fig. 6), as predicted for a 2D island nucleation mechanism. The average perpendicular growth rate for individual crystals measured in 6.0–8.0 mM urate solutions typically fell within a range of 1.4–4.3 nm s^{-1}.

Morphology evolution

We sought to more closely analyze several of the smallest and earliest formed MSU crystals using scanning electron

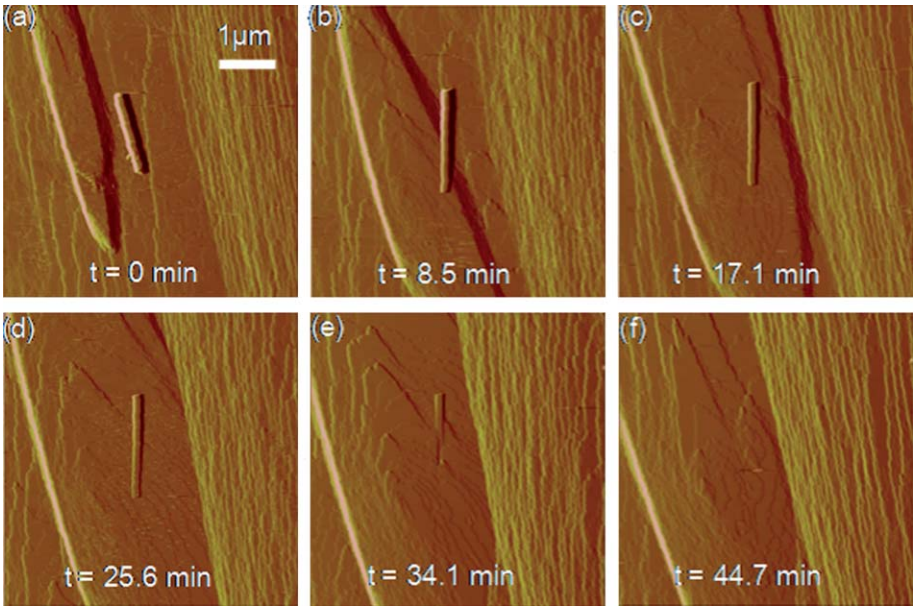

Fig. 5 Time-resolved *in situ* topographical image sequence of a MSU (010) surface growing in 6 mM urate/150 mM NaCl at 37 °C. The island reorients when it encounters a growth hillock (b), before ultimately being overgrown in subsequent images (d–f).

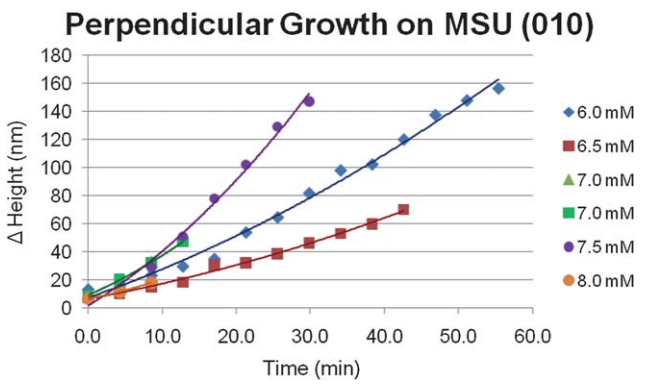

Fig. 6 Measured growth velocity normal to the MSU (010) surface. Data were obtained from six separate crystals imaged in 6–8 mM urate solutions. The increase in crystal height follows a second order polynomial relationship with time, as predicted for a 2D nucleation mechanism.

microscopy (SEM) as well as AFM imaging, in order to assess whether morphologies of newly formed and mature MSU crystals exhibit any notable differences over time. From polarized light microscopy and topographical AFM imaging, we know that macroscopic MSU crystals display only (010), (001), (1$\bar{1}$0), and (100) faces. In contrast, MSU islands ≤2 μm deposited onto growing MSU crystals exhibit triangular end facets.

Step heights imaged on the island in Fig. 7 correspond with (010). The (1$\bar{1}$0) and (100) side faces were unambiguously assigned based on the angle each face makes with the (001) surface, 87.47° and 79.56°, respectively (calculated angles = 87.87° and 79.77°). With the *a* and *b* axes established through the side faces, assigning Miller indices to the end facets was accomplished with the help of WinXMorph.[34] The best fit corresponded to facets with ($\bar{2}$11) and (5$\bar{1}$1) indices. The angles between end facets and the side faces were surprisingly consistent over several crystals examined, though higher order index assignments may be possible in some cases. These facets eventually disappear during subsequent growth to larger sizes, presumably due to their kinetic or thermodynamic instability. Interestingly, while other authors[15] have predicted additional theoretical faces from the periodic bond chain (PBC) theory, (011), (101), (1$\bar{1}$1), and (111), these do not correspond to the facets observed. Another interesting feature apparent in AFM island images is the frequent twinning observed along (100). This is also commonly observed in macroscopic crystals.

SEM imaging was also employed in an effort to better visualize the tips of mature MSU needles (Fig. 8). MSU needles are too small to be individually transferred by the scalpel blade, so SEM

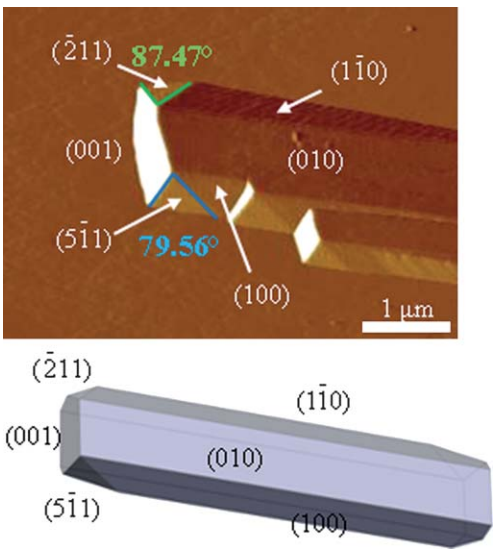

Fig. 7 (Top) Macroscopic and microscopic face assignment of adsorbing islands on the topographical AFM image (scale bar = 1 μm). (Bottom) WinXMorph model of the MSU island.

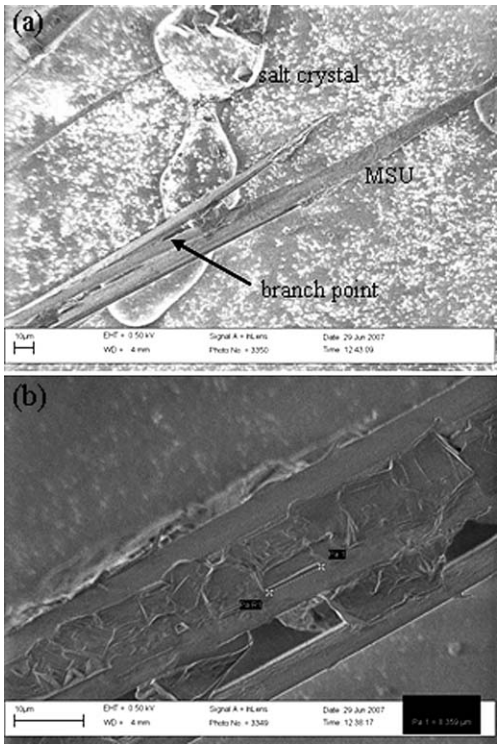

Fig. 8 SEM analysis of MSU crystal showing a branch point, indicative of twinning or secondary nucleation. MSU crystals are accompanied by evaporated drops containing salt crystals.

samples were prepared by transferring a liquid drop containing many MSU crystals to the conductive adhesive. After about a minute, the remaining solution was wicked away, leaving MSU crystals behind. The broad (010) face was visible, along with two other side faces, although it was not possible to unambiguously assign them as (100) and (1$\bar{1}$0). Faceting at the ends of MSU needles was not observed; however, most MSU crystals exhibited tapered jagged crystal edges and several branching off points from the main crystal which are likely indicative of fishtail twinning or secondary nucleation.

Conclusions

In summary, the complementary techniques of dynamic light scattering and *in situ* atomic force microscopy were employed to gain a better understanding of monosodium urate monohydrate crystallization under model conditions. DLS yielded evidence for the presence of MSU particles in 2–10 mM urate/150 mM NaCl solutions, while AFM topographical images provided a molecular-level view of the MSU (010) surface under these same conditions. The DLS particle sizes and size of adsorbed islands seen with AFM compare favorably. The spontaneous appearance of islands on the crystal surface was commonly observed. These islands typically align with the underlying substrate and can have clear faceting with high Miller indices, which are not present in macroscopic crystals. The latter suggests that the absolute morphology may be sensitive to either supersaturation, growth time, or both. These studies afford a molecular-level insight into the fundamentals of MSU crystallization and provide a comparison point to which future growth experiments in more complex fluids can be compared. Although the urate concentrations employed in this study are above the clinically relevant definition of hyperuricemia, we believe that the insight gained may be a useful step toward the development of a more comprehensive understanding and/or surface-based therapeutic strategies in the management of gout.

Acknowledgements

The authors are grateful for the financial support from the National Science Foundation (CHE 0809684, DMR 0348955 and DMR 0521170), the Clare Booth Luce Foundation (CMP predoctoral fellowship) and Georgetown University (MAD undergraduate GUROP fellowship).

References

1 M. D. Harris, L. B. Seigel and J. A. Alloway, *Am. Fam. Physician*, 1999, **59**, e1.
2 A. J. Luk and P. A. Simkin, *Am. J. Manag. Care*, 2005, **11**, s435.
3 F. Martinon and L. H. Glimcher, *J. Clin. Invest.*, 2006, **116**, 2073.
4 J. B. Wyngaardren and W. N. Kelley, *Gout and Hyperuricemia*, Grune & Stratton, Inc., New York, 1976.
5 M. Underwood, *Br. Med. J.*, 2006, **332**, 1315.
6 N. Dalbeth and D. O. Haskard, *Rheumatology (Oxford, U. K.)*, 2005, **44**, 1090.
7 B. Finlayson and A. J. Smith, *J. Chem. Eng. Data*, 1974, **19**, 94.
8 J. R. Pittman and M. H. Bross, *Am. Fam. Physician*, 1999, **59**, e1.
9 P. D. Calvert, R. W. Fiddis and N. Vlachos, *Colloids Surf.*, 1985, **14**, 97.
10 D. J. Allen, G. Milosovich and A. M. Mattocks, *J. Pharm. Sci.*, 1965, **54**, 383.
11 C.-Y. Lam Erwin and G. H. Nancollas, *J. Cryst. Growth*, 1981, **53**, 215.
12 K. Kaneko and M. Maru, *Anal. Biochem.*, 1999, **281**, 9.
13 W. R. Wilcox, A. Khalaf, A. Weinberger, I. Kippen and J. R. Klineberger, *J. Cryst. Growth*, 1973, **20**, 227.
14 A. Margalit, K. L. Duffin, A. F. Shaffer, S. A. Gregory and P. C. Isakson, *Inflammation*, 1997, **21**, 205.
15 C. Rinaudo and R. Boistelle, *J. Cryst. Growth*, 1982, **57**, 432.
16 D. J. McCarty and J. S. Faires, *Curr. Ther. Res.*, 1963, **5**, 284.
17 Z. Wang and E. Konigsberger, *Thermochim. Acta*, 1998, **310**, 237.
18 R. E. Sours, A. Z. Zellelow and J. A. Swift, *J. Phys. Chem. B*, 2005, **109**, 9989.
19 R. S. Abendan and J. A. Swift, *Cryst. Growth Des.*, 2005, **5**, 2146.
20 T. Jung, X. Sheng, C. K. Choi, W.-S. Kim, J. A. Wesson and M. D. Ward, *Langmuir*, 2004, **20**, 8587.
21 S. Guo, M. D. Ward and J. A. Wesson, *Langmuir*, 2002, **18**, 4284.
22 S. R. Qiu, A. Wierzbicki, C. A. Orme, A. M. Cody, J. R. Hoyer, G. H. Nancollas, S. Zepeda and J. J. De Yoreo, *Proc. Natl. Acad. Sci. U. S. A.*, 2004, **101**, 1811.
23 J. D. Rimer, Z. An, Z. Zhu, M. H. Lee, D. S. Goldfarb, J. A. Wesson and M. D. Ward, *Science*, 2010, **330**, 337.
24 B. J. Frisken, *Appl. Opt.*, 2001, **40**, 4087.
25 P. J. Patty and B. J. Frisken, *Appl. Opt.*, 2006, **45**, 2209.
26 N. S. Mandel and G. S. Mandel, *J. Am. Chem. Soc.*, 1976, **98**, 2319.
27 A. G. Fam, H. R. J. Schumacher, G. Clayburne, M. Sieck, N. S. Mandel, P. T. Cheng and K. P. Pritzker, *J. Rheumatol.*, 1992, **19**, 780.
28 Y. G. Kuznetsov, A. J. Malkin and A. McPherson, *Phys. Rev. B: Condens. Matter*, 1998, **58**, 6097.
29 A. S. Parmar, P. E. Gottschall and M. Muschol, *Biophys. Chem.*, 2007, **129**, 224.
30 P. G. Vekilov, *Cryst. Growth Des.*, 2004, **4**, 671.
31 O. Gliko, N. Neumaier, M. Fischer, I. Hasse, A. Bacher, S. Weinkauf and P. G. Vekilov, *J. Cryst. Growth*, 2005, **275**, e1409.
32 O. Galkin and P. G. Vekilov, *Proc. Natl. Acad. Sci. U. S. A.*, 2000, **97**, 6277.
33 O. Galkin, K. Chen, T. L. Nagel, R. E. Hirsch and P. G. Vekilov, *Proc. Natl. Acad. Sci. U. S. A.*, 2002, **99**, 8479.
34 W. Kaminsky, *J. Appl. Crystallogr.*, 2005, **38**, 566.